Effective forcing for direct numerical simulations of the shear layer of turbulent free shear flows

Chandru Dhandapani,* Kyupaeck Jeff Rah, and Guillaume Blanquart
California Institute of Technology, Pasadena, California 91125, USA

(Received 20 December 2017; published 28 August 2019)

A numerically efficient configuration to simulate turbulent flows is to use triply periodic domains, with numerical forcing techniques to sustain turbulence. Previous homogeneous shear turbulence simulations considered only idealized homogeneous shear flows and not the statistically stationary shear turbulence observed in practical free shear flows. In contrast, the current study mathematically derives the complete forcing technique from the large scales of the turbulent free shear flows. Different statistically stationary free shear flows are considered in this study, namely, a nearly homogeneous shear turbulent flow, turbulent mixing layer, a turbulent planar jet, and a turbulent round jet. The simulations are performed on triply periodic, statistically homogeneous cubic domains in the vicinity of the shear layer in the self-similar region. An *a priori* analysis is performed to calculate the effects of the different forcing terms and to predict the expected turbulence quantities. The forcing technique is then used to perform direct numerical simulations at different Reynolds numbers. Numerical results for the different cases are discussed and compared with results from experiments and other simulations of free shear turbulent flows. Anisotropy is observed both in the components of velocity and vorticity, with stronger Reynolds number dependence in the anisotropy of vorticity. Energy spectra obtained from the present homogeneous shear turbulence agree well with the spectra from temporally evolving shear layers. The results also highlight the effects of the additional forcing terms that were neglected in previous studies and the role of shear convection and the associated splitting errors in the unbounded evolution of previous numerical simulations.

DOI: 10.1103/PhysRevFluids.4.084606

I. INTRODUCTION

Turbulent free shear flows are found in a multitude of industrial applications and in nature, and their analysis gives a lot of insight into turbulence and its structure. However, owing to the range of scales and the stochastic and unsteady nature of turbulence, simulating such flows has proven to be quite challenging. Various configurations have been used to simulate turbulent flows using direct numerical simulations (DNS), which are resolved down to the smallest turbulent lengths scales.

The most obvious configuration is to use the entire domain to solve the spatially evolving flow [1–3]. In this configuration, the turbulence statistics reach a stationary state after a transient period, and hence the results are ultimately independent from the initial conditions. Unfortunately, the overall flow field depends strongly on the boundary conditions. These simulations typically include a near-field region where the turbulence is not fully developed, and so this configuration is not

*cdhandap@caltech.edu

computationally efficient. Since the entire flow field needs to be solved, these simulations are usually performed at lower Reynolds numbers to reduce the computational costs.

Another configuration is to consider temporally evolving turbulent flows. A perfect example is the mixing layer simulation by Rogers and Moser [4], which introduces homogeneity in the streamwise direction. The extra periodic direction increases the computational efficiency, but at the expense of physics. It also aids in calculating the energy spectra, which can be used to observe the different scales of turbulence. Unfortunately, the statistics never reach a stationary state, and hence the results still depend heavily on the initial conditions.

The third configuration is that of a triply periodic domain where the turbulence statistics are homogeneous and there are no boundary conditions to implement because of the triple periodicity. A good example is the numerical simulation of isotropic turbulence by Orszag and Patterson [5]. The computational efficiency is much higher as the flow is fully turbulent throughout. However, in the absence of mean shear, the turbulent kinetic energy in the domain decays over time due to viscous dissipation [6]. Hence, to keep the turbulent kinetic energy stationary over time, the missing mean shear needs to be emulated through a method of forcing the turbulence. Turbulence in the past has been forced by different techniques, including spectral forcing [7–10] and linear forcing [11–13]. While these techniques are required to generate turbulence in the domain, these numerical forcing techniques have been mostly arbitrary, and do not capture the physics of the large scale flows accurately.

Recently, Rah *et al.* [14] combined the numerical tractability of the third configuration with the physical accuracy of the first configuration. They used a triply periodic computational domain, with the forcing calculated from the flow physics at a small region at the centerline of a turbulent round jet, and forcing turbulence in a mathematically consistent way. The current study extends this work by considering a small region in the self-similar shear layer of multiple statistically stationary free-shear flows and using a triply periodic computational domain to simulate this shear-dominated flow.

Several homogeneous shear turbulence (HST) simulations have been performed in the literature using similar techniques [15–21]. While a shear production term was included in each study, considering an idealized homogeneous shear flow, the forcing terms were not derived for practical turbulent flows, and ultimately lacked the mathematical background to be compared to realistic turbulent flows. Most of these simulations use shear periodic boundary conditions, but simulate idealized homogeneous shear flow and the turbulence statistics are not stationary [16–20]. Some simulations include a wall boundary in the cross-stream direction, and are not homogeneous [21].

By simulating only the velocity fluctuations, the simulations of the current study aim to obtain the elusive combination of homogeneity and statistical stationarity in homogeneous shear turbulence calculations.

In Sec. II, the forcing technique will be mathematically derived, and then calculated, from locations in the shear layers of four different turbulent flows shown in Fig. 1. An *a priori* analysis will be performed for the forcing technique in Sec. III to observe the effects of the different forcing terms. Section IV describes the simulations, and contains a discussion of the numerical results and comparison with experiments and other simulations. Section V includes additional simulations including linear diagonal terms, nonlinear terms, and mean advection terms. Section VI makes concluding remarks about the observations from the study.

II. MATHEMATICAL DERIVATION

We start by reviewing Lundgren's mathematical approach, which uses a Reynolds decomposition to identify the effects of the large turbulent scales on the small scales. Then, four canonical flows are considered (see Fig. 1), and the forcing matrix is calculated for each of them. A forcing technique, common to the self-similar shear layer of these four flows, is discussed after.

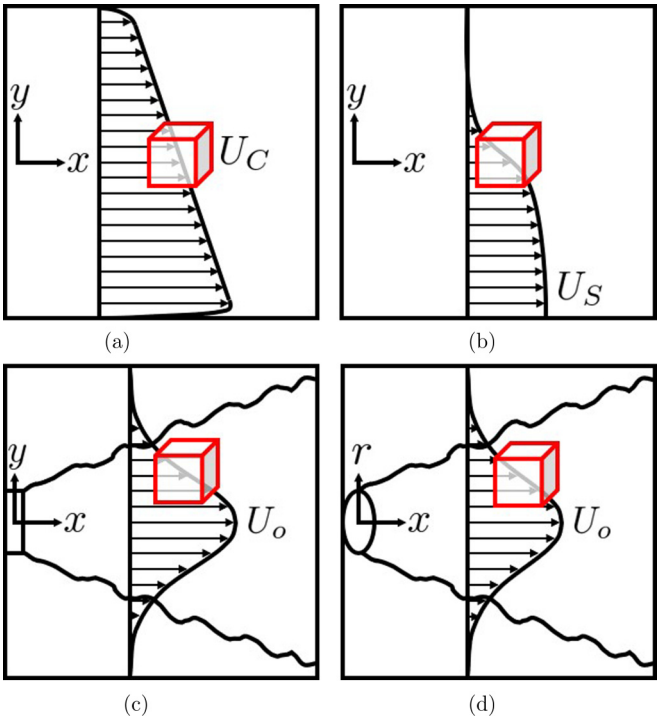

FIG. 1. Different turbulent free shear flows considered for the current study with the computational domain chosen (red cube): (a) nearly homogeneous shear turbulence (NHST), (b) mixing layer (ML), (c) planar jet (PJ), (d) round jet (RJ).

A. Methodology: Review of Lundgren's approach

First, we consider the Navier-Stokes (NS) equations for the velocity field $\boldsymbol{u}$ for a fluid flow with constant density ρ, where p is the pressure and ν is the kinematic viscosity,

$$\frac{\partial \boldsymbol{u}}{\partial t} + \boldsymbol{u} \cdot \boldsymbol{\nabla} \boldsymbol{u} = -\frac{1}{\rho} \boldsymbol{\nabla} p + \nu \nabla^2 \boldsymbol{u}. \tag{1}$$

For any turbulent flow phenomenon, the instantaneous velocity field can be decomposed into mean and fluctuating velocity fields (i.e., Reynolds decomposition), $\boldsymbol{u} = \overline{\boldsymbol{u}} + \boldsymbol{u}'$, where $\overline{\cdot}$ represents the ensemble average. Transport equations for the fluctuations are obtained by calculating the difference between the NS equations for the full velocity field and the transport equations for the mean velocity field, namely,

$$NS(\overline{\boldsymbol{u}} + \boldsymbol{u}') - \overline{NS(\overline{\boldsymbol{u}} + \boldsymbol{u}')}. \tag{2}$$

This leads to

$$\frac{\partial \boldsymbol{u}'}{\partial t} + (\overline{\boldsymbol{u}} + \boldsymbol{u}') \cdot \boldsymbol{\nabla} \boldsymbol{u}' = -\frac{1}{\rho} \boldsymbol{\nabla} p' + \nu \nabla^2 \boldsymbol{u}' + \boldsymbol{\nabla} \cdot \overline{\boldsymbol{u}' \boldsymbol{u}'} - \boldsymbol{u}' \cdot \boldsymbol{\nabla} \overline{\boldsymbol{u}}. \tag{3}$$

The extra terms in the transport equations for the fluctuating velocity, when compared with Eq. (1), are the mean-flow advection term ($\overline{\boldsymbol{u}} \cdot \boldsymbol{\nabla} \boldsymbol{u}'$), the divergence of the Reynolds stress term ($\boldsymbol{\nabla} \cdot \overline{\boldsymbol{u}' \boldsymbol{u}'}$), and the production term ($-\boldsymbol{u}' \cdot \boldsymbol{\nabla} \overline{\boldsymbol{u}}$). Lundgren focused on the production term as the only contributor to turbulent kinetic energy production [11], but this is not the case as will be seen later in section C. The major contribution to the turbulent kinetic energy comes from the production

term, which is rewritten as a forcing term $\mathbf{A} \cdot \boldsymbol{u}'$,

$$\frac{\partial \boldsymbol{u}'}{\partial t} + \boldsymbol{u}' \cdot \nabla \boldsymbol{u}' = -\frac{1}{\rho}\nabla p' + \nu \nabla^2 \boldsymbol{u}' + \mathbf{A} \cdot \boldsymbol{u}', \tag{4}$$

where $\mathbf{A}$ is the forcing matrix, given by $\mathbf{A} = -\nabla \overline{\boldsymbol{u}}$. The source term is linear in $\boldsymbol{u}'$, forces velocity along all scales, and keeps the turbulent kinetic energy from decaying due to viscous dissipation.

Lundgren [11] further assumed that the forcing matrix, $\mathbf{A}$ is a diagonal matrix that generates isotropic turbulence,

$$\mathbf{A}_{\text{Lundgren}} = \begin{bmatrix} A & 0 & 0 \\ 0 & A & 0 \\ 0 & 0 & A \end{bmatrix}. \tag{5}$$

This isotropic forcing term was implemented as $A\boldsymbol{u}'$, where A is an arbitrary forcing constant, calculated based on the required turbulent Reynolds number [13]. In practice, the forcing matrix depends on the gradients of the mean velocity.

B. Mean velocity gradients

Different free shear flows are considered in this study, namely a nearly homogeneous shear turbulence (NHST) flow, a turbulent mixing layer (ML), a turbulent planar jet (PJ), and a turbulent round jet (RJ). The mean velocity gradients can be calculated from the mean velocity profiles obtained from experiments, for each free shear flow. Once again, the intent is to perform simulations on triply periodic, statistically homogeneous cubic domains in the vicinity of the shear layer in their respective self-similar region as shown in Fig. 1.

1. Nearly homogeneous shear turbulence

For a homogeneous shear turbulence flow, the mean flow is in the streamwise direction (x). The freestream velocity is constant along x and varies linearly in y, away from the walls located at $y = -h/2$ and $y = h/2$. The mean streamwise velocity at the center of the wind tunnel, $y = 0$ is U_C. Far downstream, the quantities are self-similar and are homogeneous in the y direction away from the walls. However, the integral length scale ℓ increases linearly with x [22], and consequently, the Reynolds stresses and the velocity fluctuation magnitudes increase with x, hence the name "nearly" homogeneous shear turbulence. Equation (3) for the HST flow in the center of the wind tunnel becomes

$$\frac{\partial \boldsymbol{u}'}{\partial t} + \boldsymbol{u}' \cdot \nabla \boldsymbol{u}' = -\frac{1}{\rho}\nabla p' + \nu \nabla^2 \boldsymbol{u}' - \frac{\partial \overline{u}_x}{\partial y} u_y' \boldsymbol{e_x} - \overline{u}_x \frac{\partial \boldsymbol{u}'}{\partial x} + \frac{\partial \overline{u_x' u_x'}}{\partial x} \boldsymbol{e_x} + \frac{\partial \overline{u_x' u_y'}}{\partial x} \boldsymbol{e_y}. \tag{6}$$

Most simulations of homogeneous shear turbulence use periodic boundary conditions in the x direction without rescaling the velocity, and choose to neglect the divergence of the Reynolds stress terms. The forcing matrix for NHST at $y = 0$ is

$$A_{\text{NHST}} = -\begin{bmatrix} 0 & \frac{\partial \overline{u}_x}{\partial y} & 0 \\ 0 & 0 & 0 \\ 0 & 0 & 0 \end{bmatrix} = B_{\text{NHST}} \begin{bmatrix} 0 & 1 & 0 \\ 0 & 0 & 0 \\ 0 & 0 & 0 \end{bmatrix}. \tag{7}$$

The only element of the forcing matrix is due to the shear strain rate $\frac{\partial \overline{u}_x}{\partial y}$, and the matrix is normalized by that quantity.

2. Mixing layer

For a spatial mixing layer, the mean flow is primarily in the streamwise direction (x). The freestream velocity is constant along x, and is 0 for $y \to +\infty$ and U_S for $y \to -\infty$. The center of the

shear layer is at $y_{1/2}$, where the mean streamwise velocity is $U_S/2$. Far downstream, the mixing layer quantities are self-similar and are only a function of the similarity variable, $\eta \equiv [y - y_{1/2}(x)]/\delta(x)$. The mixing layer thickness δ increases linearly with x, and $y_{1/2}$ is linear in x [23]. There is no mean flow in the spanwise direction ($\overline{u}_z = 0$) and the flow is statistically homogeneous in the spanwise direction ($\frac{\partial \overline{u}_x}{\partial z} = 0$ and $\frac{\partial \overline{u}_y}{\partial z} = 0$).

Equation (3) at the center of the mixing layer becomes,

$$\frac{\partial \boldsymbol{u}'}{\partial t} + \boldsymbol{u}' \cdot \nabla \boldsymbol{u}' = -\frac{1}{\rho}\nabla p' + \nu \nabla^2 \boldsymbol{u}' - \frac{\partial \overline{u}_x}{\partial x} u_x' \boldsymbol{e_x} - \frac{\partial \overline{u}_x}{\partial y} u_y' \boldsymbol{e_x} - \frac{\partial \overline{u}_y}{\partial x} u_x' \boldsymbol{e_y} - \frac{\partial \overline{u}_y}{\partial y} u_y' \boldsymbol{e_y} - \overline{u}_x \frac{\partial \boldsymbol{u}'}{\partial x} - \overline{u}_y \frac{\partial \boldsymbol{u}'}{\partial y} + \frac{\partial \overline{u_x' u_x'}}{\partial x} \boldsymbol{e_x} + \frac{\partial \overline{u_x' u_y'}}{\partial x} \boldsymbol{e_y}. \tag{8}$$

The forcing matrix for the spatial mixing layer at $y = y_{1/2}$ is

$$A_{\mathrm{ML}} = -\begin{bmatrix} \frac{\partial \overline{u}_x}{\partial x} & \frac{\partial \overline{u}_x}{\partial y} & 0 \\ \frac{\partial \overline{u}_y}{\partial x} & \frac{\partial \overline{u}_y}{\partial y} & 0 \\ 0 & 0 & 0 \end{bmatrix} = B_{\mathrm{ML}} \begin{bmatrix} -0.035 & 1 & 0 \\ -0.001 & 0.035 & 0 \\ 0 & 0 & 0 \end{bmatrix}, \tag{9}$$

calculated from the mean velocity profile given by Lumley [24]. The largest element of the forcing matrix is due to the shear strain rate $\frac{\partial \overline{u}_x}{\partial y}$, and the matrix is normalized by $B_{ML} = -\frac{\partial \overline{u}_x}{\partial y}(y_{1/2}) = 1.022\frac{U_S}{\delta}$.

3. Planar jet

In a planar jet, the mean flow is primarily in the streamwise direction (x), and the centerline mean velocity at the jet axis, $U_o(x)$, decays along x as $1/\sqrt{x}$ [1,25–27]. The mean velocities are self-similar far from the jet exit, and when normalized by the centerline velocity, are only functions of the similarity variable, $\eta \equiv y/y_{1/2}(x)$, where $y_{1/2}$ is the half-width of the jet defined by $\overline{u}_x[x, y_{1/2}(x)] = U_o(x)/2$.

The jet has no mean flow in the spanwise coordinate (z), and no mean gradients along z. The forcing matrix for the planar jet in the middle of the shear layer at $y = y_{1/2}$ is calculated from mean velocity profiles given by Bradbury [25],

$$A_{\mathrm{PJ}} = -\begin{bmatrix} \frac{\partial \overline{u}_x}{\partial x} & \frac{\partial \overline{u}_x}{\partial y} & 0 \\ \frac{\partial \overline{u}_y}{\partial x} & \frac{\partial \overline{u}_y}{\partial y} & 0 \\ 0 & 0 & 0 \end{bmatrix} = B_{\mathrm{PJ}} \begin{bmatrix} -0.071 & 1 & 0 \\ -0.007 & 0.071 & 0 \\ 0 & 0 & 0 \end{bmatrix}, \tag{10}$$

where $B_{\mathrm{PJ}} = 0.730\frac{U_o}{y_{1/2}}$. Once again, the largest contribution to the forcing matrix comes from the off-diagonal shear strain term. The forcing matrix is comparable to the mixing layer forcing matrix in Eq. (9).

4. Round jet

For a round jet, Eq. (3) is rewritten in cylindrical coordinates for simplicity. The mean flow is primarily in the streamwise direction (x), and the mean centerline velocity $U_o(x)$ has a $1/x$ dependence [2,28–31]. We recall the flow is self-similar and the jet quantities, when normalized by the centerline velocity, are only functions of the similarity variable $\eta \equiv r/r_{1/2}(x)$, where $r_{1/2}$ is the half-width of the jet.

There is no mean flow in the azimuthal direction (θ), and no mean gradients along θ. Hence, the forcing matrix for the round jet in the middle of the shear layer at $r = r_{1/2}$ as shown in Fig. 1(d) is

calculated from mean velocity profiles taken from Schlichting [32],

$$A_{\mathrm{RJ}} = -\begin{bmatrix} \frac{\partial \overline{u}_x}{\partial x} & \frac{\partial \overline{u}_x}{\partial r} & 0 \\ \frac{\partial \overline{u}_r}{\partial x} & \frac{\partial \overline{u}_r}{\partial r} & 0 \\ 0 & 0 & \frac{\overline{u}_r}{r} \end{bmatrix} = B_{\mathrm{RJ}} \begin{bmatrix} -0.014 & 1 & 0 \\ -0.001 & 0.037 & 0 \\ 0 & 0 & -0.023 \end{bmatrix}, \tag{11}$$

where $B_{\mathrm{RJ}} = 0.586 \frac{U_o}{r^o_{1/2}}$. Once again, the largest element in the matrix is the off-diagonal shear strain $\frac{\partial \overline{u}_x}{\partial r}$. The matrix is comparable to the velocity gradient matrix for planar jets from Eq. (10).

C. Additional source terms

In addition to the mean velocity gradients, there are source terms that arise from enforcing periodic boundary conditions in the simulation domain [14]. The velocity fluctuations are appropriately normalized to ensure that their second order statistics are homogeneous, so periodic boundary conditions can be used, and these normalizations result in additional source terms. Although these source terms can be calculated for any of the canonical flows mentioned before, the turbulent round jet case is considered for the following calculations, as it has been researched in literature in greater detail.

1. Periodicity in x

As mentioned earlier, in a round jet, the centerline velocity $U_o(x)$ decreases with x as $1/x$. Since the velocity fluctuations are proportional to the centerline velocity, they also decay along x as $1/x$. Under these conditions, the flow is not statistically homogeneous in the x direction, and it would be inappropriate to assume periodic boundaries. To lift this limitation, the velocity fluctuations are rescaled by the $1/x$ dependence as

$$u'_x = u^{(x)}_x \frac{x_o}{x}, \quad u'_y = u^{(x)}_y \frac{x_o}{x}, \quad u'_z = u^{(x)}_z \frac{x_o}{x}, \tag{12}$$

where $\boldsymbol{u}^{(x)}$ is the velocity fluctuation that is statistically homogeneous along x in the vicinity of $x = x_o$. This rescaling produces extra elements in the forcing matrix from the $\overline{\boldsymbol{u}} \cdot \nabla \boldsymbol{u}'$ term. At $x = x_o$, the forcing matrix due to the periodicity correction in x is given by

$$A_x = \begin{bmatrix} \frac{\overline{u}_x}{x_o} & 0 & 0 \\ 0 & \frac{\overline{u}_x}{x_o} & 0 \\ 0 & 0 & \frac{\overline{u}_x}{x_o} \end{bmatrix}. \tag{13}$$

2. Periodicity in r

The simulation assumes periodicity along r as well, but the velocity fluctuations depend on the radial distance. To maintain statistical homogeneity along r, the velocity fluctuations are rescaled by their individual r dependencies,

$$u^{(x)}_x = u^{(r)}_x \, f(\eta), \quad u^{(x)}_r = u^{(r)}_r \, g(\eta), \quad u^{(x)}_\theta = u^{(r)}_\theta \, h(\eta), \tag{14}$$

where $\boldsymbol{u}^{(r)}$ is the velocity fluctuation that is statistically homogeneous along r in the vicinity of $r = r^o_{1/2} = r_{1/2}(x_o)$. The forcing matrix due to $\overline{\boldsymbol{u}} \cdot \nabla \boldsymbol{u}'$ applied on Eq. (14) is then

$$A_r = \frac{\overline{u}_r - S\overline{u}_x}{r^o_{1/2}} \begin{bmatrix} C_1 & 0 & 0 \\ 0 & C_2 & 0 \\ 0 & 0 & C_3 \end{bmatrix}, \tag{15}$$

where $S = dr_{1/2}/dx$ is the spreading rate, $C_1 = -\frac{df}{d\eta}(1)$, $C_2 = -\frac{dg}{d\eta}(1)$, and $C_3 = -\frac{dh}{d\eta}(1)$. From the velocity fluctuations profiles from Hussein *et al.* [31], we have at $r = r_{1/2}$,

$$\begin{aligned} &\overline{u}_x = 0.5U_o, \quad \overline{u}_r = 0.014U_o, \quad S = 0.0935, \\ &C_1 = 0.517, \quad C_2 = 0.398, \quad C_3 = 0.345. \end{aligned} \tag{16}$$

3. Continuity

The original continuity equation for $\boldsymbol{u}'$ is

$$\frac{\partial u_x'}{\partial x} + \frac{1}{r}\frac{\partial (r u_r')}{\partial r} + \frac{1}{r}\frac{\partial u_\theta'}{\partial \theta} = 0. \tag{17}$$

After the normalization in x and r for periodicity [Eqs. (12) and (14)], the continuity equation for $u^{(r)}$ becomes

$$\frac{\partial u_x^{(r)}}{\partial x} + \frac{1}{r}\frac{\partial (r u_r^{(r)})}{\partial r} + \frac{1}{r}\frac{\partial u_\theta^{(r)}}{\partial \theta} = (1 - C_1)\frac{u_x^{(r)}}{x_o} + C_2\frac{u_r^{(r)}}{r_{1/2}}. \tag{18}$$

The continuity equation for $\boldsymbol{u}^{(r)}$ has two extra terms. While it is possible to solve the NS equations with additional terms in the continuity equation, it is preferable to have no source terms. That is why $\boldsymbol{u}^{(r)}$ is rewritten in terms of $\boldsymbol{u}''$, under the conditions that $\boldsymbol{u}'' = \boldsymbol{u}^{(r)}$ at $\{x_o, r_{1/2}\}$ and $\boldsymbol{u}''$ is divergence free:

$$u_x^{(r)} = u_x'' \exp\left[(1 - C_1)(x/x_o - 1)\right], \quad u_r^{(r)} = u_r'' \exp\left[C_2\left(r/r_{1/2}^o - 1\right)\right], \quad u_\theta^{(r)} = u_\theta''. \tag{19}$$

The forcing matrix due to the continuity correction is

$$A_C = \begin{bmatrix} -\frac{\overline{u}_x}{x_o}(1 - C_1) & 0 & 0 \\ 0 & \frac{S\overline{u}_x - \overline{u}_r}{r_{1/2}^o} C_2 & 0 \\ 0 & 0 & 0 \end{bmatrix}. \tag{20}$$

The complete transformation from the original velocity fluctuation $\boldsymbol{u}'$ to the statistically homogeneous, divergence-free velocity fluctuation $\boldsymbol{u}''$ is given by

$$\begin{aligned} u_x' &= u_x''\frac{x_o}{x}\, f(\eta)\, \exp\left[(1 - C_1)(x/x_o - 1)\right], \\ u_r' &= u_r''\frac{x_o}{x}\, g(\eta)\, \exp\left[C_2\left(r/r_{1/2}^o - 1\right)\right], \quad u_\theta' = u_\theta''\frac{x_o}{x}\, h(\eta), \end{aligned} \tag{21}$$

and the transport equation for $\boldsymbol{u}''$ at $\{x_o, r_{1/2}\}$ is calculated as

$$\begin{aligned} \frac{\partial \boldsymbol{u}''}{\partial t} + \boldsymbol{u}'' \cdot \nabla \boldsymbol{u}'' = &-\frac{1}{\rho}\nabla p' + \nu \nabla^2 \boldsymbol{u}'' + \mathbf{A_{RJ}} \cdot \boldsymbol{u}'' - \overline{\boldsymbol{u}} \cdot \nabla \boldsymbol{u}'' + \nabla \cdot \overline{\boldsymbol{u}''\boldsymbol{u}''} \\ &+ \left[\frac{C_1 \overline{u_r}}{r_{1/2}^o} u_x'' + \frac{C_1}{r_{1/2}^o}(u_x'' u_r'' - \overline{u_x'' u_r''})\right]\boldsymbol{e_x} + \left[\frac{\overline{u_x}}{x_o} u_x'' + \frac{1}{x_o}(u_x'' u_r'' - \overline{u_x'' u_r''})\right]\boldsymbol{e_r} \\ &+ \left[\frac{\overline{u_x}(1 - C_3)}{x_o} u_x'' + \frac{1 - C_3}{x_o}(u_x'' u_\theta'' - \overline{u_x'' u_\theta''})\right]\boldsymbol{e_\theta} \\ &+ \left[\frac{\overline{u_r}}{r_{1/2}^o} u_x'' + \frac{C_3}{r_{1/2}^o}(u_r'' u_\theta'' - \overline{u_r'' u_\theta''})\right]\boldsymbol{e_\theta} + \text{visc}, \end{aligned} \tag{22}$$

with the gradients of the normal stress in $\nabla \cdot \overline{\boldsymbol{u}''\boldsymbol{u}''}$ being exactly zero, as $\boldsymbol{u}''$ is homogeneous in magnitude. Theoretically, the gradient of the Reynolds shear stress would still exist. However, at

$r = r_{1/2}$, the correlation coeffecient, $\rho_{xr} = \overline{u'_x u'_r}/(\overline{u'_x u'_x}\ \overline{u'_r u'_r})^{1/2}$ is near constant [33], and its gradient is near zero. The additional viscous terms are negligibly small for highly turbulent flows.

The final forcing matrix is calculated as a sum of all of the contributions from Eqs. (11), (13), (15), and (20), and is given by

$$A_F = A_{\mathrm{RJ}} + A_x + A_r + A_C \simeq B_{\mathrm{RJ}} \begin{bmatrix} -0.039 & 1 & 0 \\ -0.001 & 0.117 & 0 \\ 0 & 0 & 0.038 \end{bmatrix}. \tag{23}$$

It is clear that the final forcing matrix is very close to the matrix from Eq. (11), with less than 6% difference compared to the largest element. The periodicity in x and r, and the continuity correction do not have significant contributions in the shear layer of a round jet, whereas it had significant effects at the jet axis [14].

4. Nonlinear terms

All the source terms in Eq. (23) are linear in $\boldsymbol{u}''$; but the transformation from $\boldsymbol{u}'$ to the statistically homogeneous and divergence-free $\boldsymbol{u}''$ in Eq. (21) gives rise to some nonlinear source terms owing to the term $\boldsymbol{u}' \cdot \boldsymbol{\nabla u}'$, as seen in Eq. (22). These nonlinear source terms can be written as $A_{\mathrm{NL}} \cdot \boldsymbol{u}'' - \overline{A_{\mathrm{NL}} \cdot \boldsymbol{u}''}$, where A_{NL} is given by

$$A_{\mathrm{NL}} = \begin{bmatrix} \frac{C_1}{r^o_{1/2}} u''_r & 0 & 0 \\ 0 & \frac{1-C_2}{x_0} u''_x & 0 \\ 0 & 0 & \frac{1-C_3}{x_0} u''_x + \frac{C_3}{r^o_{1/2}} u''_r \end{bmatrix}. \tag{24}$$

These terms have similar magnitudes to the linear source terms from Eqs. (13) and (15), as $\sqrt{\overline{u''^2_x}}/\overline{u}_x \simeq 0.48$ and $\sqrt{\overline{u''^2_r}}/\overline{u}_x \simeq 0.36$.

D. Summary

The simulation considers the forcing matrix calculated at $\{x, r, \theta\} = \{x_o, r^o_{1/2}, 0\}$, and hence the r-θ direction in the jet coordinates can be replaced by y and z in the cartesian coordinate system of the DNS. The velocity solved for in the simulation correspond to values at the half-width of the jet, $\{u'_x, u'_r, u'_\theta\}(x_o, r^o_{1/2}, \theta) = \{u''_x, u''_y, u''_z\}$. For simplicity, $\boldsymbol{u}''$ would be represented as $\boldsymbol{u}'$ henceforth.

Some key aspects of this derived forcing must be emphasized. First, the forcing is a direct result of the physics of the free shear turbulent flows considered; the forcing term is not arbitrary, and is derived mathematically from the large scales of the mean flow. Second, the forcing is not isotropic, which is consistent with results from experiments of free shear flows, where $\langle u'^2_x \rangle > \langle u'^2_y \rangle$ [25,31]. Third, the forcing in this case is not purely from the diagonal terms as suggested by Lundgren's isotropic turbulence, but rather dominated by an off-diagonal shear term.

Comparing with other Homogeneous Shear Turbulence (HST) simulations, where the only production term is $Bu'_y \hat{\boldsymbol{e}}_{\boldsymbol{x}}$, there are additional linear forcing terms on the diagonal due to mean velocity gradients, renormalizations to maintain periodicity in the x and y/r directions, and continuity corrections. In addition to the linear diagonal forcing terms, there are also additional forcing terms that are nonlinear in $\boldsymbol{u}'$. Finally, the mean advection term is calculated as $-\overline{\boldsymbol{u}} \cdot \boldsymbol{\nabla u}' = By \frac{\partial \boldsymbol{u}'}{\partial x}$, which has been included in past simulations. To avoid confusion with the shear strain (i.e., energy production) term, this term is referred to as shear convection.

III. A PRIORI ANALYSIS

Multiple source terms have been computed in the previous section. Their effect on the turbulence quantities can be estimated using an *a priori* analysis. Once the most dominant source terms have

been selected, the relationship between the source terms and other turbulence quantities can be established.

A. Contribution of source terms

The effect of all the source terms on the turbulence can be observed from the effects on the turbulent kinetic energy, $k = \frac{1}{2}\langle u_x'^2 + u_y'^2 + u_z'^2\rangle$ ($\langle\cdot\rangle$ represents ensemble average). The transport equation for the turbulent kinetic energy can be obtained from the velocity fluctuations transport equation as

$$\frac{dk}{dt} = \left\langle u_i' \frac{\partial u_i'}{\partial t} \right\rangle. \tag{25}$$

The turbulent kinetic energy equation for the simulation including all the additional linear and nonlinear terms and mean advection terms is given by

$$\frac{dk}{dt} = -\varepsilon + \mathcal{P} + \mathcal{P}_{\text{diag}} + \mathcal{P}_{\text{NL}} + \mathcal{P}_{\text{conv}}, \tag{26}$$

where $\varepsilon = 2\nu\langle s_{ij}s_{ij}\rangle$ is the energy dissipation rate. All other terms vanish under statistical homogeneity. The contribution by each of the terms to turbulent kinetic energy production can be calculated and compared with the most dominant shear term $\mathcal{P} = B\langle u_x'u_y'\rangle$. The contribution from the diagonal terms is calculated as

$$\frac{\mathcal{P}_{\text{diag}}}{\mathcal{P}} = \frac{-0.039B\langle u_x'u_x'\rangle + 0.089B\langle u_y'u_y'\rangle + 0.038B\langle u_z'u_z'\rangle}{B\langle u_x'u_y'\rangle}. \tag{27}$$

Using Reynolds stress values from the round jet results from Hussein *et al.* [31], $\frac{\mathcal{P}_{\text{diag}}}{\mathcal{P}} = 0.117$. The contribution from the nonlinear terms can also be calculated as

$$\frac{\mathcal{P}_{\text{NL}}}{\mathcal{P}} = \frac{0.82B\langle u_x'u_x'u_y'\rangle + 0.10B\langle u_x'u_y'u_y'\rangle}{B\langle u_x'u_y'\rangle U_o} + \frac{0.10B\langle u_x'u_z'u_z'\rangle + 0.59B\langle u_y'u_z'u_z'\rangle}{B\langle u_x'u_y'\rangle U_o}. \tag{28}$$

Using velocity triple correlation values from the round jet results from Hussein *et al.* [31], $\frac{\mathcal{P}_{\text{NL}}}{\mathcal{P}} = 0.209$. The contribution from the shear convection term is computed as

$$\frac{\mathcal{P}_{\text{conv}}}{\mathcal{P}} = \frac{B\left\langle y\frac{\partial u_x'}{\partial x}u_x' + y\frac{\partial u_y'}{\partial x}u_y' + y\frac{\partial u_z'}{\partial x}u_z'\right\rangle}{B\langle u_x'u_y'\rangle} = \frac{By\frac{\partial k}{\partial x}}{B\langle u_x'u_y'\rangle}. \tag{29}$$

Because of statistical homogeneity in the x direction, $\frac{\mathcal{P}_{\text{conv}}}{\mathcal{P}} = 0$. In other words, the advection by the mean term does not contribute to kinetic energy production, as mentioned earlier. Hence, the shear convection terms are not included in the current simulation. Further analyses and justifications are provided in Secs. III C and V B.

In summary, the shear strain is the most dominant term, contributing to 75% of the production of turbulent kinetic energy. The linear terms in the diagonal of the forcing matrix and the nonlinear terms contribute to 9% and 16% of the production, respectively. Similar results are obtained for mixing layers and planar jets. The off-diagonal shear strain element is at least one order of magnitude larger than the other elements in the matrix and is the major driving force for turbulence production in these aptly named free shear flows, accounting for at least 75% of the turbulent kinetic energy production.

In the current study, for a triply periodic simulation of HST, it is a good approximation to use the off-diagonal shear strain, B, as the only forcing term, with the forcing matrix given by

$$\mathbf{A}_{\text{HST}} = \begin{bmatrix} 0 & B & 0 \\ 0 & 0 & 0 \\ 0 & 0 & 0 \end{bmatrix}, \tag{30}$$

where B can be chosen based on the simulation parameters and the desired turbulent Reynolds number. While this term does not inject any external energy, it represents the injection of energy into the velocity fluctuations by the mean flow, hence it is an "effective forcing term" in the spirit of Lundgren's approach, and is henceforth referred to as a forcing term for simplicity. This is similar to conventional simulations of HST, where the off-diagonal shear strain term is the only mechanism for turbulence production [18,20]. Those studies do not include any of the linear diagonal and nonlinear forcing terms, but they include the shear convection term that does not contribute to turbulent kinetic energy.

B. Stationary-state analysis

The entire mathematical framework presented in the previous section relies on the assumption that the velocity field can be decomposed into mean and fluctuating quantities. Then, the simulations in the current study solve for the velocity fluctuations. By construction, these velocity fluctuations represent the fluctuations of the flow field in a small region of a *statistically stationary* turbulent flow. Hence, the fluctuating quantities and their related statistics *must* reach a statistically stationary state. This applies to turbulent kinetic energy, dissipation rate, Reynolds stress, and so on.

Before performing the HST simulations, the target Reynolds number of the simulation needs to be decided, so that the required grid resolution can be evaluated to fully resolve down to the smallest turbulent scales. The relationship between the forcing constant B and the Reynolds number needs to be established, to calculate the required shear strain, B. The expected eddy turnover time is also calculated from the turbulent kinetic energy and the energy dissipation rate, to determine the total simulation time. These expected turbulence quantities are estimated from the stationary state of these simulations.

The turbulent kinetic energy equation for this HST forcing, assuming spatial homogeneity, is

$$\frac{dk}{dt} = -\varepsilon + B\langle u_x' u_y' \rangle. \tag{31}$$

At statistically stationary state, the energy dissipation rate is

$$\varepsilon = B\langle u_x' u_y' \rangle. \tag{32}$$

This should be compared to the stationary state with the isotropic forcing [13],

$$\varepsilon = 2Ak. \tag{33}$$

The cross correlation in Eq. (32) can be written in terms of the turbulent kinetic energy, $\langle u_x' u_y' \rangle = \beta k$, where β is a nondimensional parameter.

The integral length scale, ℓ, is defined as

$$\ell = \frac{u_{\text{rms}}^3}{\varepsilon} = \frac{2u_{\text{rms}}}{3\beta B}, \tag{34}$$

where rms is root-mean square and

$$u_{\text{rms}} = \sqrt{\frac{2k}{3}} = \frac{3}{2}\beta B \ell. \tag{35}$$

The Taylor microscale, λ, is calculated as

$$\lambda = \sqrt{15\frac{\nu}{\varepsilon}}u_{\text{rms}}. \tag{36}$$

The expected Taylor microscale Reynolds number for HST is calculated as

$$\text{Re}_\lambda^o = \sqrt{\frac{45\beta B \ell^2}{2\nu}}. \tag{37}$$

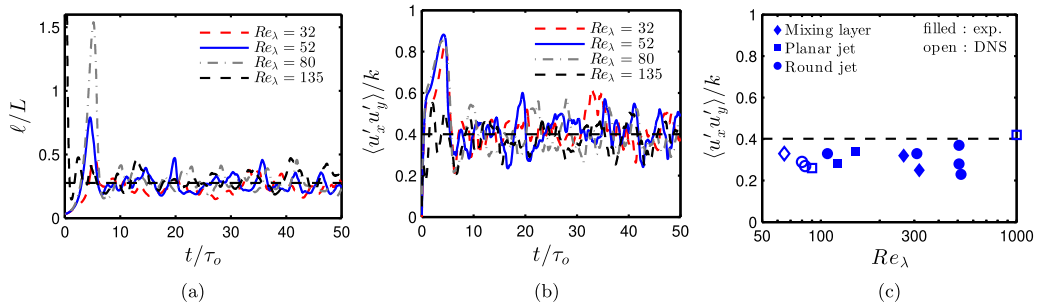

FIG. 2. (a) Integral length scale normalized by the domain width, (b) Reynolds shear stress $\langle u_x' u_y' \rangle$ normalized by turbulent kinetic energy, for the four DNS, and (c) comparison of Reynolds number dependence of Reynolds shear stress $\langle u_x' u_y' \rangle$ with other studies. Dashed lines corresponds to the averaged value obtained from all simulations in the current study.

For isotropic turbulence simulations, it was given by Carroll and Blanquart [13],

$$\mathrm{Re}_\lambda^o = \sqrt{\frac{45A\ell^2}{\nu}} \simeq \sqrt{\frac{9AL^2}{5\nu}}, \tag{38}$$

as $\ell/L \simeq 0.2$ for isotropic turbulence in a triply periodic box domain [12,13], where L is the domain width. As will be shown from numerical results in Figs. 2(a) and 2(b), $\beta \simeq 0.4$ and $\ell/L \simeq 0.28$ for HST. So, given the same domain width and viscosity, DNS of HST can be performed with the same Reynolds number as DNS of homogeneous isotropic turbulence, using the forcing constant $B \simeq 3.2A$.

The expected values for turbulent kinetic energy, k_o, and energy dissipation rate, ε_o, can be calculated as

$$k_o = \tfrac{3}{2} u_{\mathrm{rms}}^2 = \tfrac{27}{8} \beta^2 B^2 \ell^2 \tag{39}$$

and

$$\varepsilon_o = \frac{u_{\mathrm{rms}}^3}{\ell} = \frac{27}{8} \beta^3 B^3 \ell^2. \tag{40}$$

The expected eddy turnover time τ_o is given by

$$\tau_o = \frac{k_o}{\varepsilon_o} = \frac{1}{\beta B} \simeq \frac{25}{32A}, \tag{41}$$

which is slightly higher than for the isotropic case, where $\tau_o = \frac{1}{2A}$ [13].

C. Shear convection

The proposed HST simulation has a key difference from most simulations of shear turbulence [17–20]; it does not include the shear convection term $By\frac{\partial \boldsymbol{u}'}{\partial x}$. The shear convection term requires either a remeshing scheme after every few iterations [34] or implementing shear periodicity along the y direction to avoid boundary discontinuities [18–20]. It is often accomplished by using operator splitting [16,20], which may introduce further errors in the computational solution.

As mentioned earlier, the shear convection term does not contribute to turbulent kinetic energy production (see Sec. III A), as $\mathcal{P}_{\mathrm{conv}} = \langle By\frac{\partial \boldsymbol{u}'}{\partial x} \cdot \boldsymbol{u}' \rangle = 0$ due to spatial homogeneity. That being said, it may still impact the turbulent flow. To quantify this impact, we evaluate the shear strain produced by the advection term and compare it to the existing shear strain due to the turbulence. The shear strain due to the convection term can be calculated as $\frac{\partial \overline{u}_x}{\partial y} = B$ and compared against the existing

TABLE I. Simulation parameters of the different cases.

No	Re_λ^o	N^3	L	ν	B	Forcing matrix	Re_λ	u'_x/u_{rms}	u'_y/u_{rms}	u'_z/u_{rms}	$\langle u'_x u'_y\rangle/k$
1	36	64^3	2π	0.159	7.33	A_{HST}	32 ± 6	1.26	0.90	0.77	0.42
2	54	128^3	2π	0.159	16.5	A_{HST}	52 ± 9	1.23	0.93	0.78	0.41
3	80	192^3	2π	0.159	37.1	A_{HST}	80 ± 13	1.23	0.92	0.78	0.39
3a	80	192^3	2π	0.159	37.1	A_F	80 ± 15	1.21	0.94	0.79	0.39
3b	80	192^3	2π	0.159	37.1	$A_F + A_{\mathrm{NL}}$	80 ± 13	1.20	0.95	0.80	0.38
3c	80	192^3	2π	(1) 0.159 (2) −0.0159	37.1	A_{HST}	121 ± 20	1.23	0.93	0.79	0.37
3d	80	192^3	2π	0.1431	37.1	A_{HST}	85 ± 10	1.23	0.94	0.78	0.39
4	128	384^3	0.126	1.5e-5	2.77	A_{HST}	135 ± 23	1.22	0.93	0.80	0.38

shear strain due to the turbulence, $\frac{\partial u'_x}{\partial y}$. Since $\langle \frac{\partial u'_x}{\partial y}\rangle = 0$, the second-order statistics are compared as

$$\frac{B^2}{\left\langle\left(\frac{\partial u'_x}{\partial y}\right)^2\right\rangle} = \frac{\frac{15\nu}{2}B^2}{\frac{15\nu}{2}\left\langle\left(\frac{\partial u'_x}{\partial y}\right)^2\right\rangle} \simeq \frac{15\nu B^2}{2\varepsilon} = \frac{50}{\beta^2 \mathrm{Re}_\lambda^2}, \tag{42}$$

with the isotropic assumption that $\varepsilon \simeq \frac{15\nu}{2}\langle(\frac{\partial u'_x}{\partial y})^2\rangle$. For $\mathrm{Re}_\lambda = 100$, the ratio is 0.031. Hence, the impact of the shear convection term is small, and decreases with increasing Reynolds number. Thus, the shear convection term is omitted for true spatial homogeneity and numerical efficiency. Its impact will be discussed in Sec. V B.

IV. NUMERICAL RESULTS

A. Simulation

Direct numerical simulations of homogeneous shear turbulence are performed in a triply periodic box domain that is statistically homogeneous in all three directions. Simulations are performed with a domain width of $L = 2\pi$, and various Reynolds numbers Re_λ.

The simulations are performed using NGA [35], a semi-implicit velocity solver with an energy-conserving finite difference scheme on a standard staggered grid. The code solves the Navier-Stokes equations with the derived source term from Eq. (30) for constant density, temperature, and viscosity.

The initial velocity fields are generated randomly, using the method suggested by Eswaran and Pope [7]. These velocity fields conform to a specified Passot-Pouquet energy spectrum [36] and are divergence free, as is required for constant density flows.

Multiple simulations are performed at different expected values of Re_λ. The simulation parameters for the four different cases are tabulated in Table I. Cases 1 and 2 were performed to investigate low Reynolds number effects, if any. Cases 3 and 4 are chosen so the Reynolds number is comparable to simulations and experiments, published in literature (see Table II for a full list of experimental and full domain DNS studies). More precisely, case 3 has a similar Reynolds number to cases 1 [4], 4 [1], and 8 [2] from Table II; case 4 has a Reynolds number close to cases 5 [26] and 9 [3] in Table II.

The simulations were performed for a total of 50 eddy turnover times, during which the simulations were stable. The average values for the numerical results were calculated in the range, $10\tau_o$ to $50\tau_o$.

TABLE II. Anisotropy results from various experiments and simulations of different free shear turbulent flows. Average values of $u_i'/u_{\rm rms}$ and $\langle u_x' u_y' \rangle / k$ in the middle of shear layers of ML, PJ, and RJ.

No.	Case	Authors	Re_λ	$u_x'/u_{\rm rms}$	$u_y'/u_{\rm rms}$	$u_z'/u_{\rm rms}$	$\langle u_x' u_y' \rangle / k$
1	Mixing layer simulations	Rogers and Moser [4]	60–69	1.10	0.88	1.01	0.33
2	Mixing layer experiments	Oster and Wygnanski [37]	155	1.15	0.93	0.91	0.32
3	Mixing layer experiments	Wygnanski and Fiedler [38]	186	1.13	0.88	0.97	0.25
4	Planar jet simulations	Stanley *et al.* [1]	89–92	1.05	1.02	0.92	0.26
5	Planar jet experiments	Gutmark and Wygnanski [26]	122	1.33	0.75	0.81	0.28
6	Planar jet experiments	Bradbury [25]	148–154	1.15	0.93	0.90	0.34
7	Planar jet calculations	Pope [27]	–[a]	1.28	0.85	0.81	0.42
8	Round jet simulations	Boersma *et al.* [2]	80	1.21	0.84	0.92	0.29
9	Round jet simulations	Wang *et al.* [3]	113	1.21	0.90	0.85	0.27
10	Round jet experiments	Panchapakesan and Lumley [29]	172	1.23	0.86	0.86	0.33
11	Round jet experiments	Falchi and Romano [39]	232	1.21	0.88	0.88	–
12	Round jet experiments	Burattini *et al.* [40]	309	1.29	0.82	0.82	0.33
13	Round jet experiments	Hussein *et al.* [31] LDA	508	1.17	0.88	0.92	0.28
		Hussein *et al.* [31] HWA		1.20	0.84	0.92	0.37
14	Round jet experiments	Wygnanski and Fiedler [41]	520	1.22	0.86	0.88	0.23

[a]Planar jet calculations were performed by Pope using a Monte Carlo method to solve the joint probability density function equation. These results correspond to the high Reynolds number limit and are plotted at $\mathrm{Re}_\lambda = 1000$ in Figs. 2(c) and 4(b). These values agree very well with results from the current study.

B. Temporal evolution

Since the configuration is periodic in all three directions, and spatially homogeneous, ensemble averaged mean quantities are calculated as spatial averages ($\langle \cdot \rangle$). These spatial averages are plotted as a function of time.

The time evolution of the integral length scale is plotted in Fig. 2(a), and after an initial transient period of at most $10\tau_o$ gives a mean value of about $0.28L$, which is slightly higher than the $0.2L$ for isotropic turbulence observed by Rosales and Meneveau [12]. The integral length scale reaching a statistically stationary value of the order of the domain width is consistent with past simulations of statistically stationary homogeneous shear turbulence [42].

Since the largest gradient of the mean flow is the shear strain $\frac{\partial \overline{u}_x}{\partial y}$, the only significant Reynolds stress term is $\langle u_x' u_y' \rangle$. This is reflected by the simulation, as the forcing term is in the equation for the axial velocity (u_x'), proportional to the cross-stream velocity (u_y'). So, it is expected that u_x' and u_y' have a significant positive correlation. This is one of the major differences between HIT and HST, as there is no correlation among the velocities in different directions for the isotropic case. Figure 2(b) shows the $\langle u_x' u_y' \rangle$ values normalized by k at different Re_λ. It can be seen that after $5\tau_o$, the values fluctuate around 0.4 for all cases, in good agreement with each other.

The average value of Reynolds shear stress from all simulations of the current study is also plotted in Fig. 2(c) and compared with values from various simulations and experiments plotted as a function of Reynolds number. The current study overpredicts the Reynolds shear stress, by about $1.5\,\sigma$ compared to values from other studies, and there seems to be no clear dependence on Re_λ.

The turbulent kinetic energy and energy dissipation rate, normalized by their respective expected values calculated from Eqs. (39) and (40), are plotted versus time for the different cases in Fig. 3. The values fluctuate around the expected values, so the estimation of k_o and ε_o are accurate. The fluctuations increase in magnitude with increasing Reynolds number. This is expected, as linear forcing becomes more unstable with higher Reynolds number, as observed by Carroll and Blanquart [13], who used a modification to the linear forcing term to improve stability. In contrast, the current

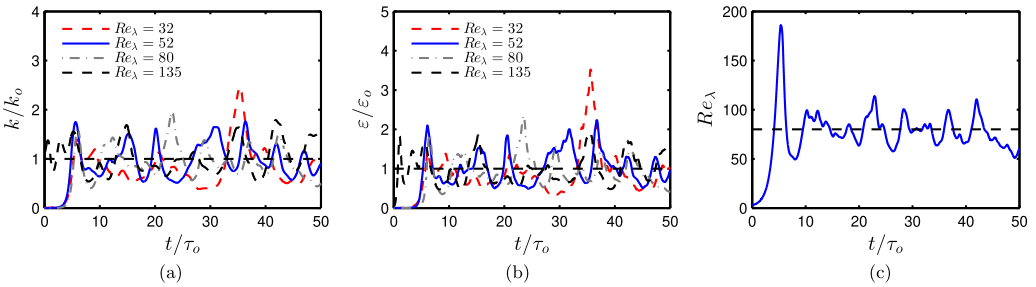

FIG. 3. (a) Turbulent kinetic energy normalized by its expected value [Eq. (39)]. (b) Energy dissipation rate normalized by its expected value [Eq. (40)]. (c) Taylor microscale Reynolds number, Re_λ, for DNS 3. Dashed line corresponds to $\mathrm{Re}_\lambda^o = 80$.

forcing term uses constant mean shear, as opposed to the constant production forcing used by Carroll and Blanquart [13].

Figure 3(c) shows the Reynolds number, based on Taylor microscale, versus time for case 3, and it can be observed that Re_λ fluctuates around the expected value (80, in this case) after a transient period of about $5\tau_o$.

C. Anisotropy

Second-order statistics can be analyzed to gather information about the velocity fluctuations and consequently about the turbulence. The magnitudes of the velocity fluctuation components ($|u_x'|$, $|u_y'|$, and $|u_z'|$) are calculated from the rms of the fluctuating velocity components (e.g., $|u_i'| = \sqrt{\langle u_i'^2 \rangle}$). Because of the anisotropic nature of free shear flows, it is expected that the velocity fluctuations will be larger in magnitude along the axial direction. This is corroborated by other simulations and experiments in Table II, and is reflected in the forcing. Although the forcing is only along the axial direction, turbulence redistributes some of the fluctuations to the other directions, while maintaining higher fluctuations in the axial direction.

Figure 4(a) plots the velocity fluctuation components along the x, y, and z directions normalized by u_{rms} for $\mathrm{Re}_\lambda^o = 80$. For isotropic turbulence, velocity fluctuations are expected to be similar along all directions, and hence $|u_i'|/u_{\mathrm{rms}} \simeq 1$. For HST, as expected, the axial direction has the largest

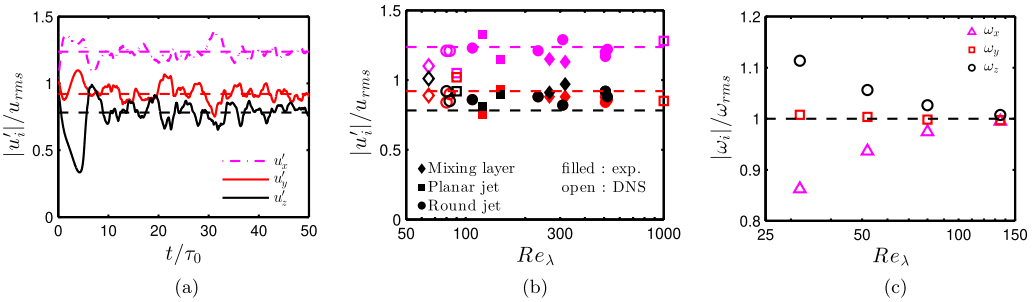

FIG. 4. (a) Root-mean-square velocity components along x, y, and z, normalized by u_{rms}, for DNS 3 ($\mathrm{Re}_\lambda^o = 80$). (b) Mean values for velocity fluctuations normalized by u_{rms} from other studies plotted versus Re_λ. Dashed lines correspond to the averaged values from the current simulations (1.24, 0.92, and 0.78, respectively). (c) Average values of rms vorticity components along different directions normalized by ω_{rms} plotted versus Re_λ. Dashed line corresponds to isotropic turbulence. (a) Anisotropy in velocity, (b) Re_λ dependence of anisotropy, and (c) Anisotropy in vorticity.

fluctuations, and the cross-stream direction and spanwise direction have smaller fluctuations. The results follow the same trend for all Reynolds numbers considered. The average values from the four cases of our current study are $|u'_x|/u_{\rm rms} \simeq 1.25$, $|u'_y|/u_{\rm rms} \simeq 0.91$ and $|u'_z|/u_{\rm rms} \simeq 0.78$.

The average values of rms velocity components are plotted in Fig. 4(b), along with data from multiple simulations and experiments of mixing layers, planar jets, and round jets, plotted versus Reynolds number. The current simulation solves for $\boldsymbol{u}''$, and from Eq. (21), $\boldsymbol{u}'' = \boldsymbol{u}'$ at x_o, $r^o_{1/2}$. Therefore, the spatially averaged results of the current study can be compared against temporally-averaged values in the middle of shear layers. All of the free shear flows seem to agree well with each other. The results from the current study agree reasonably well with the values from literature within $1\,\sigma$, except for $|u'_z|/u_{\rm rms}$, where the current study underpredicts the values, by $2\,\sigma$. Also, there seem to be no Reynolds number effects on the velocity fluctuation magnitudes, as the values remain constant across a large range of Re_λ.

The anisotropy in the smallest turbulent length scales can be observed using the root-mean square of the vorticity components ($|\omega_x| = \sqrt{\langle\omega_x^2\rangle}$, etc.), normalized by the rms vorticity, $\omega_{\rm rms} = \sqrt{\langle\boldsymbol{\omega}\cdot\boldsymbol{\omega}\rangle/3}$. Kolmogorov suggested that at very high Reynolds number, the turbulence is isotropic at the smallest turbulent length scales and hence, the vorticity would be statistically isotropic with $|\omega_i| \simeq \omega_{\rm rms}$. As shown in Fig. 4(c) and as expected, the averaged vorticity magnitudes reach isotropic values with increasing Reynolds numbers.

D. Energy spectrum

The one-dimensional energy spectra for the velocity are calculated from the simulation results of DNS 1–4. Leveraging the flow homogeneity, energy spectra are calculated using one-dimensional Fourier transforms in the x direction, $[\mathcal{F}_1(\boldsymbol{u})]$ in space at different times during the simulations, $E(\kappa_1) = \mathcal{F}_1(\boldsymbol{u})\cdot[\mathcal{F}_1(\boldsymbol{u})]^*$ versus the wave number in the x direction, κ_1, where $\cdot^*$ represents the complex conjugate. The final spectrum plotted in Fig. 6(a) is calculated as the mean of the spectra from all data files from $10\tau_o$ to $50\tau_o$, at time intervals of $0.5\tau_o$ for data independence. Figure 6(a) shows the energy spectra of all the four simulations. The spectra are normalized by the Kolmogorov length and velocity scales and show a collapse at all wave numbers. The four spectra follow well the $\kappa_1^{-5/3}$ spectrum expected from turbulence simulations.

As mentioned earlier, the conditions of DNS 4 were selected to match the DNS of Rogers and Moser [4]. Rogers and Moser performed a simulation of a temporally evolving mixing layer using a Galerkin spectral method with $512 \times 210 \times 192$ Fourier modes. They reported one-dimensional energy spectra in x_1 (streamwise) and x_3 (spanwise) calculated at a Reynolds number of $\mathrm{Re}_m \simeq 2000$. The one-dimensional spectra, $E(\kappa_1)$ and $E(\kappa_3)$, are calculated for DNS 4 and plotted in Fig. 5, where $E(\kappa_3) = \mathcal{F}_3(\boldsymbol{u})\cdot[\mathcal{F}_3(\boldsymbol{u})]^*$, where $\mathcal{F}_3(\boldsymbol{u})$ is the one-dimensional Fourier transform of the velocity in the z direction. The one-dimensional spectra, $E(\kappa_1)$ and $E(\kappa_3)$, follow that $\int E(\kappa_i)d\kappa_i = \langle u'^2_x + u'^2_y + u'^2_z\rangle = 2k$, $i = 1, 3$ and are plotted versus wave number in the two directions κ_1 and κ_3. It is seen that $E(\kappa_1)$ and $E(\kappa_3)$ are nearly indistinguishable, and these plots agree well with the spectra from Rogers and Moser [4]. Note that the ranges of wave numbers are different between the two simulations, because of different domain sizes and resolutions. This spectral analysis shows that the simulations reproduce shear-driven turbulence in the spectral sense as well.

E. Production spectrum

Finally, the one-dimensional spectra for the turbulent kinetic energy production are calculated from the shear stress spectra. The shear stress spectrum, $E_{12}(\kappa_1)$ is calculated from the same data files as the energy spectrum, as $E_{12}(\kappa_1) = 0.5\{\mathcal{F}_1(u_x)\cdot[\mathcal{F}_1(u_y)]^* + \mathcal{F}_1(u_y)\cdot[\mathcal{F}_1(u_x)]^*\}$ such that $\int E_{12}(\kappa_1)d\kappa_1 = \langle u'_x u'_y\rangle$. The production spectra are plotted versus wave number in Fig. 6(b). The wave number and the spectra are normalized with B and Kolmogorov length and velocity scales, $u_\eta = (\nu\varepsilon)^{1/4}$, and the spectra show a collapse at all wave numbers.

It is seen that the production spectra scale as $\kappa_1^{-7/3}$ as suggested by Lumley [24]. The production spectra decay faster than the energy spectra, which scale like $\kappa_1^{-5/3}$. Hence, the production to energy

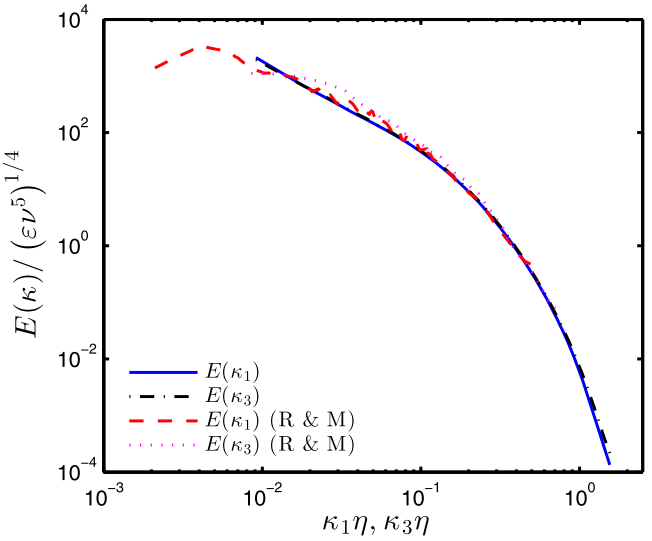

FIG. 5. Comparison of one-dimensional energy spectra along x and z directions. R & M refers to the energy spectra published by Rogers and Moser [4].

ratio is higher in the large scales, and gets smaller approaching the small scales. In contrast, linear isotropic turbulence forces velocity proportional to the energy among all scales [11,13] and most spectral techniques only force velocity over a low wave-number bandwidth [7–10].

V. ADDITIONAL CONSIDERATIONS

As mentioned earlier, all of these simulations were performed with a single off-diagonal forcing term. However, the additional diagonal terms from the velocity gradients and the diagonal and nonlinear terms from the periodicity and continuity corrections can also be included in the simulation as forcing terms. The impact of these additional forcing terms are analyzed by comparing the simulations with and without them.

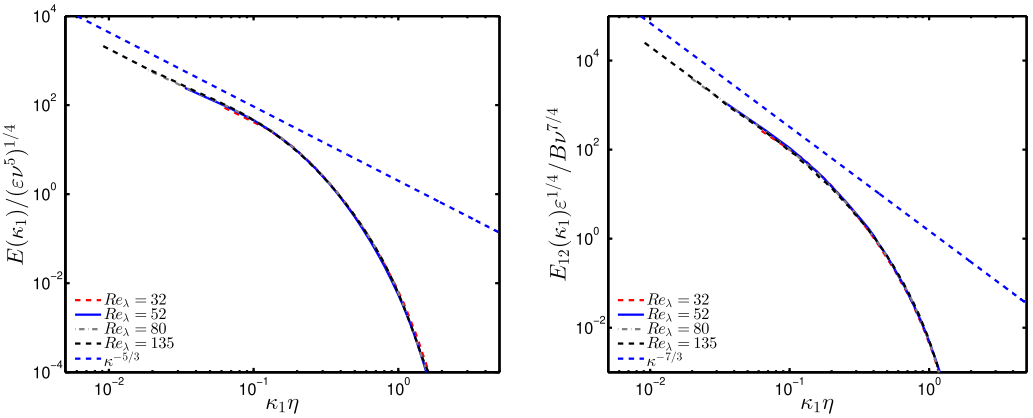

FIG. 6. (a) Energy spectra normalized by ε and ν. (b) Shear stress spectra normalized by ε and ν. The dashed line corresponds to turbulence scaling from literature, $\kappa^{-5/3}$ in (a) and $\kappa^{-7/3}$ in (b).

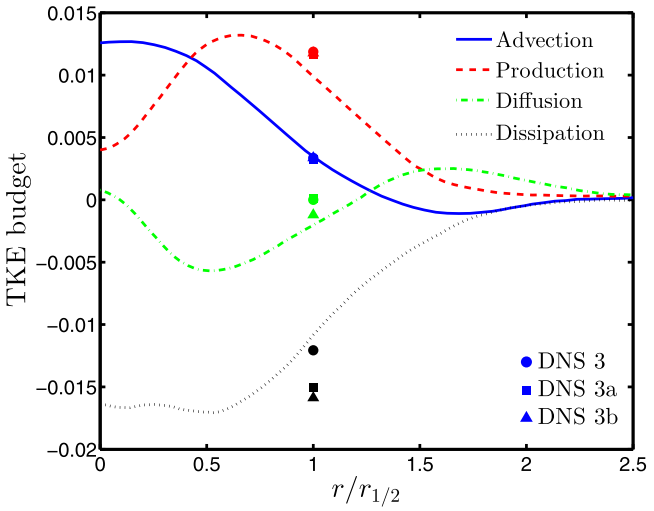

FIG. 7. Normalized turbulent kinetic energy budget. The lines correspond to experimental results from Panchapakesan and Lumley [29]. Symbols correspond to different simulations: DNS3, circles; DNS 3a, triangles; DNS 3b, squares.

A. Linear diagonal and nonlinear source terms

Simulation 3 was repeated as DNS 3a with all the linear diagonal terms from Eq. (23) and as DNS 3b with all linear and nonlinear terms from Eq. (24). This second simulation is the closest representation to the half-width of the turbulent round jet.

1. Anisotropy and energy production

DNS 3a gives an average value of $\langle u_x' u_y' \rangle = 0.39$ and DNS 3b gives an average value of $\langle u_x' u_y' \rangle = 0.38$, which are both very close to the results from DNS 3. The diagonal terms only contribute to about 7% of the turbulent kinetic energy production, and the nonlinear terms are responsible for 12% of it in DNS 3b. These results are slightly less than our *a priori* estimate of the contributions (see Sec. III A). The off-diagonal term is the major contributor to the production, accounting for 93% and 81% of the kinetic energy production in DNS 3a and 3b, respectively.

2. Turbulent kinetic energy budget

The various terms in the budget of the turbulent kinetic energy, namely the production, advection, turbulent diffusion, and the dissipation, are calculated and compared against the turbulent kinetic energy budget for the turbulent round jet. The current simulations correspond to the location of the half-width of the round jet, and should be compared against the experimental values at $r = r_{1/2}$.

The budget values are plotted in Fig. 7 and compared with the experiment results of Panchapakesan and Lumley [29]. The forcing matrix from the velocity gradients corresponds to production, $\text{Prod} = \langle \boldsymbol{u}' \cdot \nabla \overline{\boldsymbol{u}} \cdot \boldsymbol{u}' \rangle = \langle \boldsymbol{u}' \cdot A_G \cdot \boldsymbol{u}' \rangle$; the diagonal elements of the forcing matrix from the renormalization matrices A_x and A_r correspond to advection, $\text{Adv} = \overline{\boldsymbol{u}} \cdot \nabla k = \langle \boldsymbol{u}' \cdot A_x \cdot \boldsymbol{u}' \rangle + \langle \boldsymbol{u}' \cdot A_r \cdot \boldsymbol{u}' \rangle$; and the turbulent diffusion can be calculated from the triple correlation, $\text{Diff} = \nabla \cdot \langle \boldsymbol{u}' k \rangle = \langle k u_y' \rangle / r_{1/2} + 3 \langle k u_x' \rangle / x_o$. The dissipation rate is calculated as $\text{Diss} = -\varepsilon$. These quantities are calculated from the three simulations, regardless of what the forcing matrix is. All the values are normalized by $U_o^3 / r_{1/2}$, where U_o is calculated as $U_o = \sqrt{k/0.062}$ [31] and $r_{1/2}$ is calculated as $r_{1/2} = 0.586 U_o / B$ [32].

As expected, the major contributions to the budget are from production and dissipation, and the advection and diffusion are closer to zero. The advection by the mean is accurately represented

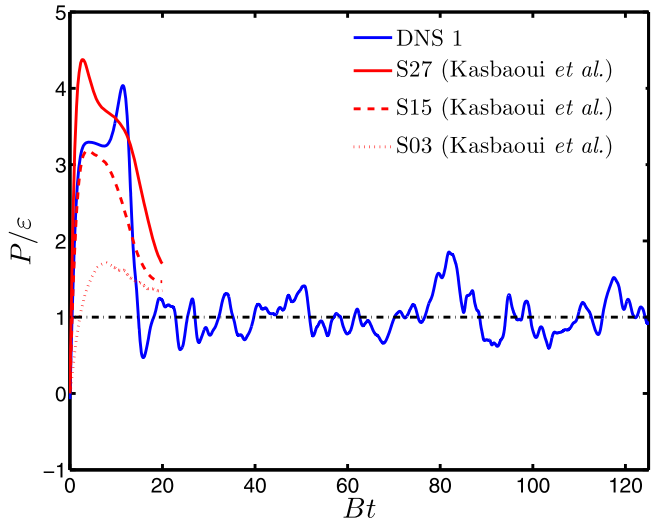

FIG. 8. Ratio of production to dissipation of kinetic energy. The blue line corresponds to simulations in the current study and the three lines correspond to three simulations by Kasbaoui *et al.*, with different initial conditions.

by the simulation, whereas the production and dissipation are slightly over-predicted. This result is consistent with the over-prediction of the shear Reynolds stress $\langle u_x' u_y' \rangle$ [see Fig. 2(c)], and the dissipation increasing to match the turbulent kinetic energy production. The diffusion value of case 3b matches fairly well with the experimental results, as they include nonlinear source terms which appear as diffusion terms (triple correlations) in the kinetic energy budget, while case 3 and 3a show zero diffusion. Apart from this, there are very small differences between the simulations without the diagonal terms (case 3), with the diagonal terms (case 3a), and with the nonlinear terms (case 3b). In fact, the dissipation values from DNS 3 are closer to the experimental results. Hence, adding the additional source terms do not make any improvement in the turbulent kinetic energy budget, except in the turbulent diffusion.

The simulations involve a balance between the two major contributors, production and dissipation. As seen in Fig. 8, the ratio of production to dissipation of kinetic energy fluctuates around a value of 1.0 (for our DNS), after an initial increase. The current simulation method focuses only on the velocity fluctuations and by definition has to be statistically stationary in the long term. This is in fact true as the simulation is stable in the long term, and reaches a stationary state where production and dissipation balance each other. The simulations by Kasbaoui *et al.,* however, had to be stopped at $Bt = 20$, because of the exponential growth of the kinetic energy, where P/ε ratio is much higher than 1 for all the simulations [20]. While being higher than 1, the ratio of P/ε in all three cases have the general same evolution and seem to tend toward unity.

3. Velocity correlations

The velocity correlation between u_x' and u_y' is analyzed by plotting their joint probability density function (pdf). Contour plots of the probability density function at different velocity fluctuation values are shown in Fig. 9. High probability is found near small values of the velocity fluctuations, and a positive correlation is observed from the positive tilt of the contours. There seems to be few discernible differences between the simulations with only the off-diagonal term (case 3), and with additional diagonal and nonlinear terms (case 3b). The key difference is in the skewness of the velocity component toward the negative values, and the maximum being away from the origin for case 3b.

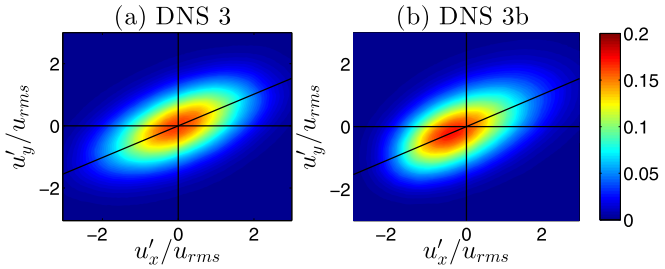

FIG. 9. Joint pdf of the normalized velocity fluctuations in the x and y directions from simulation with (a) just the off-diagonal term and (b) linear and nonlinear terms.

The marginal pdf of the velocity fluctuations in the x and y directions are plotted in Fig. 10. It was verified that the mean of the velocity fluctuations are zero, despite the high skewness observed in the results of DNS 3b. The velocity fluctuations in the x direction (u'_x) show larger differences between the two simulations. The normalized skewness and flatness for DNS 3 are $\langle u''^3\rangle/\langle u''^2\rangle^{1.5} = -0.03$ and $\langle u''^4\rangle/\langle u''^2\rangle^2 = 2.83$, respectively, while for DNS 3b gives 0.41 and 3.06, respectively. The differences are less prominent in velocity fluctuations in the y direction (u'_y). The skewness and flatness values are -0.01 and 3.02 for DNS 3 and 0.26 and 3.14 for DNS 3b, respectively. The skewness values from DNS 3b are comparable to those calculated from the experiments of Hussein *et al.* [31], 0.37 for u'_x and 0.45 for u'_y, and Panchapakesan and Lumley [29], 0.44 for u'_x and 0.39 for u'_y. The flatness values for both simulations are near 3.0, which is the flatness for normal distributions.

B. Advection by the mean

As mentioned in Sec. III, homogeneous shear turbulence has been simulated in the past using the off-diagonal production term (Bu'_y), and the advection by the mean term ($By\frac{\partial u'}{\partial x}$). The production term has been included in all the simulations in the current study. The mean advection is represented by the renormalization matrices, A_x and A_r as forcing terms, and captured correctly in the turbulent kinetic energy budget (see Sec. V A 2). The only effect missing is the straining induced by the mean flow [17–20].

Multiple studies have performed sheared turbulence simulations by including the shear convection term, but do not reach long term stability and as a result, usually run only until $Bt = 28$ or lower [17–20,43]. Kasbaoui*et al.*'s [20] study represents one of the best cases of the past studies, reaching $Bt = 20$, which corresponds to $t/\tau_o = 8$ in our case. Their simulations of sheared turbulence also

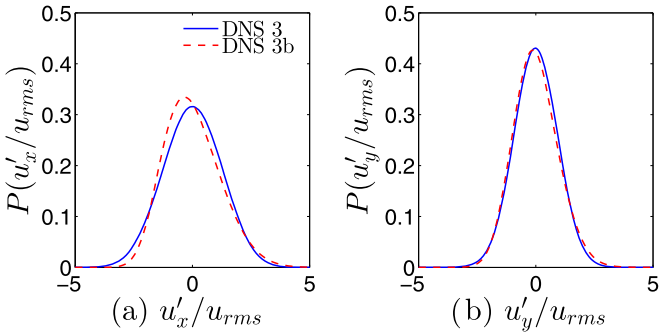

FIG. 10. Marginal pdf of the normalized velocity fluctuations in the (a) x and (b) y directions from simulation with just the off-diagonal term, and linear and nonlinear terms.

TABLE III. Turbulence quantities before and after shear remapping.

	$\boldsymbol{u}_1$			$\boldsymbol{u}_2$			Drop
Re_λ^o	k/k_o	$\langle u_x' u_y' \rangle / k$	$\varepsilon/\varepsilon_o$	k/k_o	$\langle u_x' u_y' \rangle / k$	$\varepsilon/\varepsilon_o$	in ε
36	0.842	0.430	1.018	0.842	0.432	0.876	13.9%
54	0.972	0.415	1.139	0.972	0.415	0.984	13.5%
80	0.918	0.394	0.955	0.918	0.394	0.865	9.4%
128	1.019	0.381	0.997	1.019	0.381	0.910	8.7%

include the shear convection term, which was implemented using operator splitting. Only a brief description of the multi-step procedure is given here. The reader is referred to Ref. [20] for more details. Step 1 starts with the velocity vector $\boldsymbol{u}^n$, and the momentum equation is solved with the production term included, resulting in $\overline{\boldsymbol{u}}$, referred to as $\boldsymbol{u}_1$ henceforth. Then, step 2 is to apply the shear-remapping, by $\breve{\boldsymbol{u}}(\boldsymbol{x}) = \boldsymbol{u}_1(\boldsymbol{x} - By\Delta t)$ and apply a pressure correction, to get $\boldsymbol{u}^{n+1}$ which is divergence free, referred to as $\boldsymbol{u}_2$. The boundary conditions in the y direction are shear periodic, such that $f(x, L_y, z) = f(x - BtL_y, 0, z)$.

The simulations in our current study solve for the momentum equation with the production term, hence the velocity field corresponds to $\boldsymbol{u}_1$. To quantify the effect of step 2, the shear convection term is applied *a posteriori*. Specifically, the velocity field is convected in the x direction proportional to the distance in the y direction from the bottom of the domain. The time step ΔT is chosen such that the difference in displacement at $y = 0$ and $y = L_y$ is exactly one grid point, that is $BL_y\Delta T = \Delta x$. This time step was of similar magnitude and slightly higher than the time step per iteration, Δt, in the current study. The pressure correction is then applied to obtain the divergence-free velocity field, $\boldsymbol{u}_2$.

The turbulence quantities are calculated from the original data files (corresponding to the velocity field after step 1, $\boldsymbol{u}_1$) and from the shifted data files (corresponding to the velocity field after step 2, $\boldsymbol{u}_2$ using appropriate boundary conditions). The average quantities are summarized in Table III. As expected (see Sec. III A), the turbulent kinetic energy and the Reynolds shear stress are not affected at all. The only change observed is a reduction in the viscous dissipation rate, ε, by about 8–14%. The drop in ε decreases with increase in Reynolds number, which is consistent with the *a priori* analysis of shear convection (see Sec. III C).

The effect of shear convection on the turbulent kinetic energy can be emulated by decreasing the viscous dissipation rate in two different ways. First and to be consistent with the splitting procedure of Kasbaoui *et al.* [20], a new simulation DNS 3c is performed, where step 1 is to solve the momentum equation with the production term ($\nu_1 = \nu$) and step 2 is to solve the equation,

$$\frac{\partial \boldsymbol{u}''}{\partial t} = \nu_2 \nabla^2 \boldsymbol{u}'', \tag{43}$$

with $\nu_2 = -0.10\nu$. This emulates the shear convection term with the operator splitting aspect, where solving the momentum equation and the shear convection are executed as different steps. While these methods likely do not capture all the physical effects of the shear convection, it aims to emulate the biggest effect of shear convection on the turbulence statistics.

Alternatively, if there were no operator splitting and all the operations were to be performed in one step, it would correspond to solving the momentum equation with the production term, and an effective viscosity, $\nu_{\text{eff}} = \nu_1 + \nu_2 = 0.90\nu$. DNS 3d is performed under these conditions, which correspond to the same parameters as DNS 3 with $\nu = 0.1431$ instead of 0.159. Figure 11 shows the evolution of kinetic energy from the three simulations, DNS 3, DNS 3c, and DNS 3d. Unsurprisingly, DNS 3 and 3d are very similar. Effectively, DNS 3d is a simulation with the pure shear and only a different viscosity, i.e., a different Reynolds number. However, when shear convection is emulated with operator splitting, the evolution of the turbulent kinetic energy is

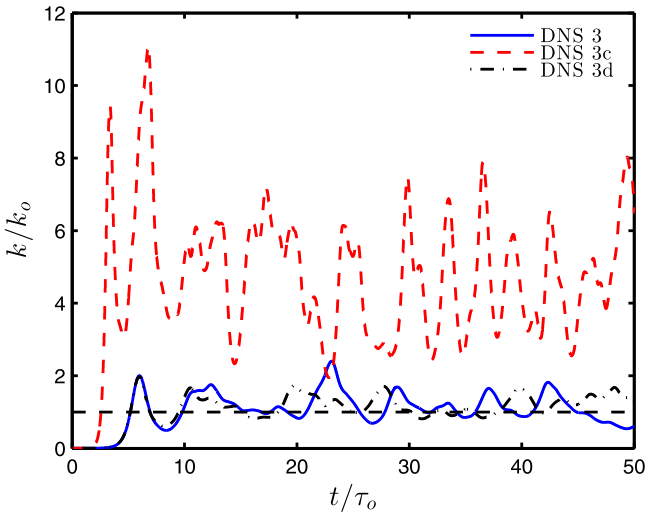

FIG. 11. Evolution of turbulent kinetic energy normalized by the expected value [Eq. (39)] for different treatment of the shear convection term.

completely different. It is striking that such a small reduction in ε (about 10%) has such a large effect on k (about 500%). From this comparison, proper care must be taken while using operator splitting, considering the numerical implications and errors associated with it.

In the current simulations, the time step per iteration, Δt is approximately equal to ΔT, the time taken for a shift by one grid point. As the actual time step, Δt is reduced, the shear convection term would be applied only every $N_s = \Delta T/\Delta t$ iterations, and its contribution would decrease linearly with decrease in Δt. This first-order error (in Δt) is consistent with Godunov-style splitting schemes.

VI. CONCLUSION

To provide a physical and mathematical foundation to realistic turbulent flows, the turbulence forcing technique for shear flows is directly computed from the large scales of these flows. Different statistically stationary free shear flows were considered for the calculations of the forcing matrix. The forcing terms did not just arise from the shear strain or the velocity gradients, but also from periodicity corrections in x, y/r, and continuity corrections, which generated both linear and nonlinear forcing terms. The additional source terms were calculated by leveraging the self-similarity of velocity fluctuations and their moments.

An *a priori* analysis was performed to estimate the effect of the multiple source terms to the turbulence, including the linear diagonal forcing terms, nonlinear forcing terms, and the mean advection term. The relation between the forcing constant and the Taylor microscale Reynolds number was established, so that turbulence quantities can be predicted prior to selecting the grid resolution for any simulation.

The turbulence generated is anisotropic in nature, consistent with that observed in the middle of shear layers. The Reynolds shear stress values are over predicted within statistical uncertainty, compared to experimental and simulation results. For the same Reynolds number, the anisotropic turbulence has higher integral length scale, lower turbulent kinetic energy and dissipation rate, and higher eddy turnover time than isotropic turbulence.

Anisotropy is observed both in the components of velocity and vorticity. The anisotropy in the fluctuating velocity agrees reasonably well with results from simulations and experiments of free shear flows. The anisotropy in the fluctuating velocity shows no clear Re_λ dependence, while the

vorticity components become more isotropic with increasing Reynolds number. The spectra for the energy and production agree with the scalings suggested by turbulence theory and past simulations.

Simulations were performed with the additional linear and nonlinear source terms, and compared with the pure shear simulations, with a special attention to Reynolds shear stress, turbulent kinetic energy budget, and velocity correlations. There was no significant difference between the two simulations with linear source terms. The simulation with all the linear and nonlinear terms showed nonzero turbulent diffusion and skewness in velocity fluctuation distributions, which were not present in the simulation with just the linear terms. In either case, the additional forcing terms did not significantly improve upon the simulation results.

The shear convection due to the mean advection term was applied *a posteriori*, and simulations were performed emulating its effect. It was observed that the effect of this term is not significant and would be negligible especially at high Reynolds number. The results also pointed out the potential role of splitting errors in previously published unbounded numerical simulations.

ACKNOWLEDGMENTS

We gratefully acknowledge financial support from the National Science Foundation. (CBET 1512771) and from the Air Force Office of Scientific Research (FA9550-16-1-0510) under the supervision of Dr. Chiping Li, and a graduate fellowship (C.D.) from the Resnick Sustainibility Institute at Caltech.

[1] S. A. Stanley, S. Sarkar, and J. P. Mellado, A study of the flow-field evolution and mixing in a planar turbulent jet using direct numerical simulation, J. Fluid Mech. **450**, 377 (2002).

[2] B. J. Boersma, G. Brethouwer, and F. T. M. Nieuwstadt, A numerical investigation on the effect of the inflow conditions on the self-similar region of a round jet, Phys. Fluids **10**, 899 (1998).

[3] Z. Wang, P. He, Y. Lv, J. Zhou, J. Fan, and K. Cen, Direct numerical simulation of subsonic round turbulent jet, Flow, Turbul. Combust. **84**, 669 (2010).

[4] M. M. Rogers and R. D. Moser, Direct simulation of a self-similar turbulent mixing layer, Phys. Fluids **6**, 903 (1994).

[5] S. A. Orszag and G. S. Patterson, Jr., Numerical Simulation of Three-Dimensional Homogeneous Isotropic Turbulence, Phys. Rev. Lett. **28**, 76 (1972).

[6] J. R. Herring and R. M. Kerr, Comparison of direct numerical simulations with predictions of two-point closures for isotropic turbulence convecting a passive scalar, J. Fluid Mech. **118**, 205 (1982).

[7] V. Eswaran and S. B. Pope, An examination of forcing in direct numerical simulations of turbulence, Comput. Fluids **16**, 257 (1988).

[8] S. Ghosal, T. S. Lund, P. Moin, and K. Akselvoll, A dynamic localization model for large-eddy simulation of turbulent flows, J. Fluid Mech. **286**, 229 (1995).

[9] D. Carati, S. Ghosal, and P. Moin, On the representation of backscatter in dynamic localization models, Phys. Fluids **7**, 606 (1995).

[10] J. R. Chasnov, Simulation of the Kolmogorov inertial subrange using an improved subgrid model, Phys. Fluids A **3**, 188 (1991).

[11] T. S. Lundgren, Linearly forced isotropic turbulence, in *Annual Research Briefs* (Center for Turbulence Research, Stanford, 2003), pp. 461–473.

[12] C. Rosales and C. Meneveau, Linear forcing in numerical simulations of isotropic turbulence: Physical space implementations and convergence properties, Phys. Fluids **17**, 095106 (2005).

[13] P. L. Carroll and G. Blanquart, A proposed modification to Lundgren's physical space velocity forcing method for isotropic turbulence, Phys. Fluids **25**, 105114 (2013).

[14] K. J. Rah, C. Dhandapani, and G. Blanquart, Derivation of a realistic forcing term to reproduce the turbulent characteristics of round jets on the centerline, Phys. Rev. Fluids **3**, 084606 (2018).

[15] M. M. Rogers and P. Moin, The structure of the vorticity field in homogeneous turbulent flows, J. Fluid Mech. **176**, 33 (1987).
[16] T. Gerz, U. Schumann, and S. E. Elghobashi, Direct numerical simulation of stratified homogeneous turbulent shear flows, J. Fluid Mech. **200**, 563 (1989).
[17] M. J. Lee, J. Kim, and P. Moin, Structure of turbulence at high shear rate, J. Fluid Mech. **216**, 561 (1990).
[18] K. A. Brucker, J. C. Isaza, T. Vaithianathan, and L. R. Collins, Efficient algorithm for simulating homogeneous turbulent shear flow without remeshing, J. Comput. Phys. **225**, 20 (2007).
[19] J. C. Isaza and L. R. Collins, On the asymptotic behavior of large-scale turbulence in homogeneous shear flow, J. Fluid Mech. **637**, 213 (2009).
[20] M. H. Kasbaoui, R. G. Patel, D. L. Koch, and O. Desjardins, An algorithm for solving the Navier–Stokes equations with shear-periodic boundary conditions and its application to homogeneously sheared turbulence, J. Fluid Mech. **833**, 687 (2017).
[21] J. Schumacher and B. Eckhardt, On statistically stationary homogeneous shear turbulence, Europhys. Lett. **52**, 627 (2000).
[22] F. H. Champagne, V. G. Harris, and S. Corrsin, Experiments on nearly homogeneous turbulent shear flow, J. Fluid Mech. **41**, 81 (1970).
[23] F. H. Champagne, Y. H. Pao, and I. J. Wygnanski, On the two-dimensional mixing region, J. Fluid Mech. **74**, 209 (1976).
[24] J. L. Lumley, Similarity and the turbulent energy spectrum, Phys. Fluids **10**, 855 (1967).
[25] L. J. S. Bradbury, The structure of a self-preserving turbulent plane jet, J. Fluid Mech. **23**, 31 (1965).
[26] E. Gutmark and I. Wygnanski, The planar turbulent jet, J. Fluid Mech. **73**, 465 (1976).
[27] S. B. Pope, Calculations of a plane turbulent jet, AIAA J. **22**, 896 (1984).
[28] P. Burattini, R. A. Antonia, and L. Danaila, Similarity in the far field of a turbulent round jet, Phys. Fluids **17**, 025101 (2005).
[29] N. R. Panchapakesan and J. L. Lumley, Turbulence measurements in axisymmetric jets of air and helium. part 1. air jet, J. Fluid Mech. **246**, 197 (1993).
[30] G. N. Abramovich, T. A. Girshovich, S. I. Krasheninnikov, A. N. Sekundov, and I. P. Smirnova, *The Theory of Turbulent Jets* (Izdatel Nauka, Moscow, 1984).
[31] H. J. Hussein, S. P. Capp, and W. K. George, Velocity measurements in a high-Reynolds-number, momentum-conserving, axisymmetric, turbulent jet, J. Fluid Mech. **258**, 31 (1994).
[32] V. H. Schlichting, Laminar beam propagation, ZAMM-J. Appl. Math. Mech. **13**, 260 (1933).
[33] S. B. Pope, *Turbulent Flows* (Cambridge University Press, Cambridge, 2001).
[34] R. S. Rogallo, Numerical experiments in homogeneous turbulence, NASA Technical Memorandum 81315 (1981).
[35] O. Desjardins, G. Blanquart, G. Balarac, and H. Pitsch, High order conservative finite difference scheme for variable density low mach number turbulent flows, J. Comput. Phys. **227**, 7125 (2008).
[36] T. Passot and A. Pouquet, Numerical simulation of compressible homogeneous flows in the turbulent regime, J. Fluid Mech. **181**, 441 (1987).
[37] D. Oster and I. Wygnanski, The forced mixing layer between parallel streams, J. Fluid Mech. **123**, 91 (1982).
[38] I. Wygnanski and H. E. Fiedler, The two-dimensional mixing region, J. Fluid Mech. **41**, 327 (1970).
[39] M. Falchi and G. P. Romano, Evaluation of the performance of high-speed PIV compared to standard PIV in a turbulent jet, Exp. Fluids **47**, 509 (2009).
[40] P. Burattini, M. Falchi, G. P. Romano, and R. A. Antonia, PIV and hot wire measurements in the far field of turbulent round jets, Meas. Sci. Technol. **21**, 125402 (2010).
[41] I. Wygnanski and H. Fiedler, Some measurements in the self-preserving jet, J. Fluid Mech. **38**, 577 (1969).
[42] A. Sekimoto, S. Dong, and J. Jiménez, Direct numerical simulation of statistically stationary and homogeneous shear turbulence and its relation to other shear flows, Phys. Fluids **28**, 035101 (2016).
[43] M. M. Rogers, P. Moin, and W. C. Reynolds, The structure and modeling of the hydrodynamic and passive scalar fields in homogeneous turbulent shear flow, Ph.D. thesis, Department of Mechanical Engineering TF-25, Stanford University, 1986.